Nanoscale

Accepted Manuscript

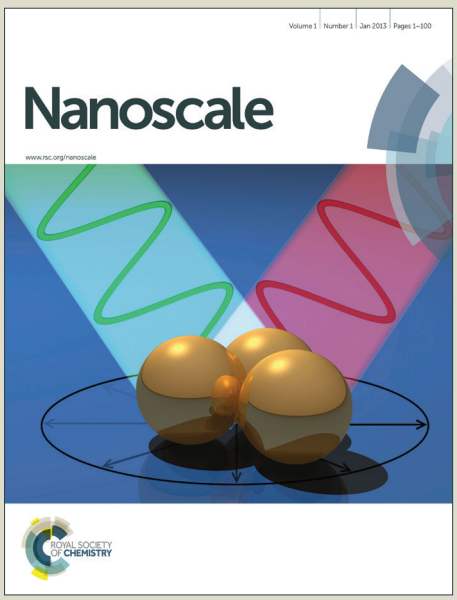

ROYAL SOCIETY OF CHEMISTRY

www.rsc.org/nanoscale

3D Graphene Supported MoO_2 for High Performance Binder-free Lithium Ion Battery

Zhi Xiang Huang, Ye Wang, Yun Guang Zhu, Yumeng Shi, Jen It Wong, and Hui Ying Yang*

Pillar of Engineering Product Development, Singapore University of Technology and Design, 20 Dover Drive, Singapore 138682

E-mail: yanghuiying@sutd.edu.sg

Abstract

In this work, we report the synthesis of MoO_2 nanoparticles grown on three dimensional graphene (3DG) via the reduction of α-MoO_3 nanobelts through a facile chemical vapor deposition (CVD) approach under Argon protection gas environment. In this synthesis approach, the presence of hydrophobic 3DG promoted the Volmer-Weber growth of MoO_2 nanoparticles (30 – 60 nm). The as-prepared MoO_2-3DG nanocomposite was directly used as a binder-free anode electrode for lithium ion batteries (LIBs) without additives, and exhibited excellent electrochemical performance. It delivered high reversible capacities of 975.4 mAh g^{-1} and 537.3 mAh g^{-1} at the current densities of 50 and 1000 mA g^{-1}, respectively. Moreover, the electrode also showed an increased capacity from 763.7 $mAhg^{-1}$ to 986.9 $mAhg^{-1}$ after 150 discharge and charge cycles at a current density of 200 mA g^{-1}. The enhanced electrochemical performance of MoO_2-3DG nanocomposite electrode may be attributed to the synergistic effects of MoO_2 nanoparticles and 3DG layers. This facile CVD synthesis process presents a feasible route for large-scale production of high performance, environmental friendly electrode. In addition, this process also has the potential of being utilized in other materials for energy storage devices application.

Keywords: MoO_2 nanoparticles, 3D graphene, binder free electrode, lithium ion batteries

1. Introduction

Lithium-ion batteries (LIBs) have dominated the power source of the portable electronics market owing to their salient features in terms of high energy density, long stable cycle life and no memory effect.[1-3] In recent years, LIBs usage has expanded into larger scale applications such as hybrid electric vehicles (HEVs), electric vehicles (EVs) and even grid-scale energy storage.[4-6] At present, commercial LIB anode material is typically graphite, which suffers from relatively low theoretical specific capacity of 372 mAh g^{-1},[7] resulting in the limitation of the further application of LIBs.[8, 9]

Research efforts to improve the performance for LIBs brought about the discovery of conversion and alloying type materials which paved new ways for the relentless search for higher capacity materials.[1, 10, 11] Among the identified materials, transition metal oxides have been of great research interests due to their significantly higher theoretical capacities than that of graphite.[12-15] In particular, nanostructured MoO_2 has received much attention owing to its high specific theoretical capacity of 838 mAh g^{-1}, reduced lithium ion diffusion distance and high stability.[16-24] However, MoO_2 has poor capacity retention due to its significant volume changes during lithiation and delithiation process.[25, 26] A common strategy to reduce the volume change is to incorporate MoO_2 with carbonaceous conductive additives such as amorphous carbon[12, 27-33], carbon nanotubes (CNT)[34], graphite oxide[35] and graphene[25, 26, 36-39]. Amongst these carbon materials, graphene is highly attractive as it offers large specific surface area and high electron mobility which greatly improve lithium ion diffusion kinetics.[38] However, graphene-based nanocomposites utilized layered graphene sheets which inevitably agglomerates and restacks due to strong $\pi - \pi$ interactions and van der Waal forces.[40, 41] As a result, the advantages of graphene are not fully exploited.

Recently, continuous interconnected three dimensional graphene (3DG) grown on nickel foam has been synthesized and employed to enhanced performance of supercapacitors and

LIBs.[40, 42-44] The 3DG does not only retain the high electrical conductivity property of graphene, but the seamless 3D network is able to support further hierarchical nanocomposites growth. In this aspect, nanomaterials can be directly deposited onto the surfaces of 3DG foam and thus creating binder-free electrodes. Traditionally, LIB electrodes are made up of active materials that are held together onto the current collector using a mixture of conductive carbon and binder. These type of LIB electrodes suffer from capacity losses when active material exfoliates from the current collector. This is typically caused the inability of the binder to withstand volume changes of the active materials during charge and discharge cycling.[45] Therefore binder-free electrodes, with active materials that are directly in physical contact with the current collector, are able to reduce the pulverization of active materials during volume changes. Furthermore, the close contact between the active materials and current collector provides a pathway for fast and efficient transport of electrons and ions between the electrolyte, active materials, and 3DG.[46]

Herein, we present a facile process to synthesize MoO_2 nanoparticles anchored on 3DG which takes advantage of the above mentioned properties of 3DG foam. The as-synthesized MoO_2-3DG nanocomposites could be directly used as LIB electrode without binder or further treatment. The binder-free electrode exhibited high capacity, long cycle life and excellent rate capabilities as a result of the synergistic effects of the MoO_2 nanoparticles and 3DG layers.

2. Experimental

2.1. Synthesis of MoO_2-3DG nanocomposites

Nickel foams (~1.2 mm in thickness) were purchased from Alantum Advanced Technology Materials (Shenyang) and all other chemical reagents were purchased from Sigma-Aldrich and used directly without further purification.

The MoO_2-3DG nanocomposite was prepared via reduction of α-MoO_3 nanobelts and deposition onto 3DG foam through a facile chemical vapor deposition (CVD) method. 3DG foam was synthesized following a previously developed method with slight modification.[43] Briefly, Ni foam was rapidly heated to 1000 ^oC at a rate of 50 $^oC\ min^{-1}$ in Ar environment. Then ethanol vapour was transported by Ar gas flow through bubbling of anhydrous ethanol for 10 min under ambient pressure. Thereafter, the sample was quickly cooled down to room temperature (~ 100 $^oC\ min^{-1}$).

The synthesis of α-MoO_3 nanobelts was consistent to the modified hydrothermal method as described by Jiang *et al*.[47] In a typical process, 5 mmol of $Na_2MoO_4{\cdot}2H_2O$ and 10 mmol NaCl were added to 40 mL of deionized (DI) water and dissolved under magnetic stirring. 10 mL of 3 M HCl was then added dropwise with continuously stirring for 10 mins. Thereafter, the final precursor was transferred into a 100 mL Teflon-line stainless steel autoclave and heated at 180 ^oC for 12 h. After the hydrothermal reaction, the autoclave was cool down to room temperature. Finally, the precipitate was collected and washed by DI water and anhydrous ethanol for 3 times to remove excess reactants and surfactant. The α-MoO_3 nanobelt powder was collected after drying the precipitate in an oven at 80 ^oC for 12 h.

In a typical procedure to synthesize MoO_2-3DG nanocomposite, 20 mg of α-MoO_3 nanobelt powder was loaded into a ceramic boat with 6 pieces of 3DG foam (12 mm diameter) and transferred into a quartz tube. Prior to heating the tube, Ar gas was flushed through for 10 min to remove air in the quartz tube. Thereafter, the tube temperature was raised rapidly at 50 $^oC\ min^{-1}$ from room temperature to 800 ^oC and kept for 10 min for MoO_2 growth, followed by cooling down to room temperature naturally.

2.2. Characterization

Powder X-ray diffraction (XRD) measurement was carried out by an X-ray diffractometer

(Siemens, D5005) equipped with a Cu Kα radiation (l≈1.54 Å). Raman spectroscopy was performed by WITec Confocal Raman Microscope alpha300 R. The morphology and structure of the products were characterized by field-emission scanning electron microscopy (FESEM) using JEOL JSM-7600F and transmission electron microscopy (TEM JEOL JEM-2010).

2.3. Electrochemical measurements

The electrochemical performance measurements were carried out by a two-electrode half-cell configuration composed of the lithium metal as the counter electrode and active material as the working electrode. The as-synthesized MoO_2-3DG nanocomposite (MoO_2: ~2 mg and 3DG: ~0.5 mg) on Ni foam was used directly used as electrode without adding of conductive materials or binder. Two control samples were prepared for further evaluation. Firstly, bulk MoO_2 powder (Sigma Alrich) was mixed with conductive carbon black and polyvinylidene fluoride (PVDF) binder in a weight ratio of 70:10:20 by adding several drops of N-Methylpyrrolidone (NMP) to prepare the electrode slurry. The slurry was then coated onto Ni foam current collector and dried in a vacuum oven at 120 ^{o}C for 12 h to form pure MoO_2 working electrodes. The second control sample was the as-prepared 3DG directly without further treatment. All working electrodes were assembled into standard CR2032 coin cells in an argon-filled glove box. Celgard 2400 membranes were used as separators and 1 M $LiPF_6$ solution in a mixture ethylene-carbonate/ethyl-methyl-carbonate (EC/EMC, 1:1 v/v) as electrolyte. Galvanostatic cycling of all the assembled half-cells were carried out in the potential range of 0.01 – 3.0 V using the Neware battery tester. Cyclic voltammetry (CV) was performed at a scan rate of 0.05 mV s^{-1} and electrochemical impedance spectra (EIS) was measured in a range of 0.01 Hz to 1 MHz on an electrochemical workstation (VMP3, Bio-Logic).

3. Results and Discussion

3.1. Morphology and structure of MoO_2-3DG

A schematic diagram of the synthesis MoO_2 nanoparticles grown onto 3DG foam substrates via a facile CVD technique is illustrated in Figure 1(a). MoO_3 nanobelts (Figure S1(a)) were volatized at high temperature (800 ^oC) and subsequently reduced to MoO_2 by carbon in graphene. The MoO_2 nucleated and grew as nanoparticles on the surface of 3DG as shown in the SEM image in Figure 1(d). Graphene layers can be observed by the crease and folds of the dark background under the uniformly distributed MoO_2 nanoparticles (30 to 60 nm) which is consistent to the as-prepared 3DG (Figure 1(b)). In contrast, MoO_2 particles grown on 3DG using bulk MoO_3 as the precursor produced particles with irregular shapes and sizes (from nanometer to micrometer), as shown in Figure S1(c) and (d), indicating that bulk MoO_3 nanobelts were less suitable than MoO_3 nanobelts for uniform MoO_2 nanoparticles growth. The growth features of the facile CVD method are highlighted (labelled 1 and 2 in Figure 1(a)) in the illustration of MoO_2 nanoparticles on graphene layer and the accompanying SEM image in Figure 1(d). Firstly, the dwell time during the synthesis was kept to a short time of 10 min in order to prevent the MoO_2 nanoparticles from coalescing into bulk microparticles. Label 1 shows the effect of the short dwell time where two nanoparticles are in close contact but yet to coalesce as can be seen by the visible grain boundary between the two particles. In contrast, the hydrophilic Ni foam allows layered growth of MoO_2 and forms large micron sized particles (Figure S1(e)) in the absence of hydrophobic graphene layers. It was also observed that excessive growth of MoO_2 resulted in cracks and signs of peeling (S1(f) and (g)). Next, label 2 shows two nanoparticles that are ~10 nm apart but do not coalesce. The evidences shown above suggest high surface tension between hydrophobic graphene layers and nucleating MoO_2 nanoparticles, indicating growth process could be a Volmer-Weber growth mechanism.[48]

High resolution TEM (HRTEM) was also employed to confirm the interaction between MoO_2 nanoparticles and 3DG layers of the as-synthesized MoO_2-3DG nanocomposites. In Figure 2(a), the lattice fringes with a spacing of 0.34 nm corresponds to the interplanar spacing of (011) crystal plane of monoclinic MoO_2. The dotted curves with lattice fringes of 0.34 nm can be identified as several layers graphene. The HRTEM image in Figure 2(b) exemplifies that the MoO_2 nanoparticles are anchored on graphene where fine nanoparticles (2 to 5 nm) wrapped by graphene sheets.

Figure 2(c) shows the XRD patterns of the precursor MoO_3 nanobelts and MoO_2-3DG. The diffraction peaks located at 26.1° and 53.7° are corresponding to (011) and (022) planes of monoclinic MoO_2 (JCPDS no. 65-1273).[29, 49] The overlapping peak at 26.1° could be assigned to (002) crystal plane of graphitic carbon (JCPDS 75-1621). The absence of other characteristic peaks of impurities or other molybdenum oxides indicates that MoO_3 nanobelts were completely reduced to MoO_2. Raman spectroscopy was performed for both MoO_2-3DG and MoO_3 nanobelts. In Figure 2(d), the Raman peaks before 800 cm^{-1} are ascribed to MoO_2 and the Raman peaks after 1300 cm^{-1} belongs to 3DG of the MoO_2-3DG nanocomposite. The Raman bands for both MoO_2 and MoO_3 are readily identified and agreed well with values reported in literature.[50, 51] This further confirms that the MoO_3 nanobelts were fully reduced into MoO_2 during the growth process. The Raman peaks located at ~1354, 1575 and 2706 cm^{-1} can be attributed to D, G and 2D bands of typical graphene layers from 3DG. The low ratio between the 2D and G bands implies that the 3DG on the Ni foam substrate consists of several layers of graphene while the low ratio between the D and G bands indicates high quality 3DG, indicating the high conductivity of 3DG in MoO_2-3DG nanocomposites.[42]

3.2. Electrochemical characterization of MoO_2-3DG

The electrochemical properties of bulk MoO_2 and as-prepared MoO_2-3DG nanocomposite electrode were investigated by CV over a range of 0.01 to 3.0 V as shown in Figure 3. In both

CV curves of Figure 3 (a) and (b), irreversible reduction peaks at around 0.3V for bulk MoO_2 electrode and 0.12V for MoO_2-3DG nanocomposite electrode was observed in the first discharge cycle, due to the formation of a solid electrolyte interface (SEI) layer at the interface of electrolyte and electrode (a polymer/gel-like film).[21, 34] In subsequent cycles, there are two sharp reversible redox couples located at 1.56/1.73 V and 1.26/1.45 V in both graphs. These two redox couples correspond to the reversible phase transformation between monoclinic and orthorhombic phases of Li_xMoO_2 and MoO_2 during the insertion and extraction process.[23, 52] The overlapping of the subsequent cycling curves in Figure 3(b) implying the good reversibility of MoO_2-3DG. It is worth mentioning that the MoO_2-3DG CV curve has two reversible redox couple at around 0.13/0.25 V, matching the redox peaks of as-prepared 3DG at around 0.17/0.24 V, which are characteristic of Li_xC phase transformation during lithium-ion insertion/extraction.[30, 36, 53] This indicates that the graphene layers are electrochemically active for lithiation/delithiation.

Figure 4(a) shows the 1st, 5th, 10th discharge/charge voltage profiles for the MoO_2-3DG nanocomposite at a current density of 50 mA g^{-1}. During the first discharge/charge cycle, the discharge and charge capacities are 1161.9 mAh g^{-1} and 921.7 mAh g^{-1}, respectively, with an initial Coulombic efficiency as high as 79.3%. The initial Coulombic efficiency of 79.3% is relatively higher than most report MoO_2-based anodes in LIB which is typically around ~70%.[31, 35, 49, 54] In subsequent charge/discharge cycles, the Coulombic efficiency increased and maintained at about 99%. In the first charge discharge cycle, two plateaus are present at around 1.28/1.4 V and 1.55/1.68 V owing to the phase transformation from MoO_2 to Li_xMoO_2.[27] However, these plateaus gradually diminishes over the next few cycles as Li_xMoO_2 converts into Mo and Li_2O.[27] Another charge plateau around 0.07/0.12 V could be attributed to the phase transformation of carbon in 3DG to Li_xC.[30, 53] All plateaus are in good agreement with the CV results.

Theoretically, 4 molar Li^+ ions can be stored per molar MoO_2 leading to a specific capacity of 838 mAh g^{-1}. However, the discharge capacities for the MoO_2-3DG nanocomposites at a current density of 50 mAh g^{-1} in the first discharge (1161.9 mAh g^{-1}) and fifth discharge (975.4 mAh g^{-1}) is substantially higher than the theoretical value. The high first discharge capacity can be attributed to the irreversible capacity arising from SEI formation coupled with the decomposition of electrolyte. In subsequent cycles, the high reversible discharge capacities could have been contributed by reversible lithium-ion binding to hydrogen terminated dangling bonds on the surface of graphene as well as phase transformation to Li_xC during intercalation.[35, 53, 55] The high reversible capacity of the nanocomposites may be described by these proposed reactions[54]:

$$MoO_{2+x} + (4 + 2x)Li^+ + (4 + 2x)e^- \leftrightarrow Mo + 2Li_2O_{(MoO_2)} + xLi_2O_{(3DG)} \quad (1)$$

$$6C + xLi \rightarrow Li_xC_6 \quad (2)$$

After 10 cycles at a current rate of 50 mA g^{-1}, the same half-cell was subjected cycled for another 150 cycles at the current density of 200 mAh g^{-1} to probe the longevity of the MoO_2-3DG nanocomposites. After 150 successive cycles, the MoO_2-3DG half-cell was able to reversibly discharge 986.9 mAh g^{-1} which is 129% more than the initial discharge capacity of 763.7 mAh g^{-1} while maintaining an average Coulombic efficiency of 98.7 % (Figure 4 (b)). The gradual increase in reversible capacities over cycles could be attributed to an activation process where partial degradation of the crystallinity of the electrode to amorphous-like structure results in an improved lithium-ion diffusion kinetics.[22] Such phenomena have been observed in several MoO_x-based and also other transition metal oxide electrode materials.[15, 27, 46, 56, 57]

For comparison, bulk MoO_2 and 3DG electrodes were fabricated and subjected to the same galvanostatic cycles. In Figure 4(c) at 200 mAh g^{-1}, it is observed that the MoO_2-3DG nanocomposites has far superior capacity and longevity as compared to bulk MoO_2 and

as-prepared 3DG. In the first cycle, bulk MoO_2 and as-prepared 3DG started off with discharge capacities of 318.7 mAh g^{-1} and 242.9 mAh g^{-1}, and ended off after 150 cycles with 92.7 mAh g^{-1} (29 % of initial) and 257.6 mAh g^{-1} (106 % of initial), respectively. In contrast, the capacity of the MoO_2-3DG nanocomposites is not only higher but also exhibits an increased capacity of 986.9 mAh g^{-1} (129 % of initial) after 150 cycles. In addition, MoO_2-3DG nanocomposites also displayed good cycling performance even at a high current density of 1000 mAh g^{-1} which is again far superior to the bulk MoO_2 and as-prepared 3DG. As shown in Figure S2(b), it was observed that throughout 100 cycles, the MoO_2-3DG nanocomposites maintained a stable discharge capacity of ~520 mAh g^{-1} as opposed to the decaying capacity of bulk MoO_2 and low capacity of as-prepared 3DG. The longevity of the MoO_2-3DG can be attributed to the morphology of MoO_2-3DG nanocomposites shown in Figure 1 and 2. The MoO_2 nanoparticles anchored on graphene is highly advantageous in LIB application as charge transport and transfer can take place rapidly across the conductive graphene layers to the nanoparticles. Furthermore, the graphene layers acts as an elastic buffer which is capable of accommodating volume changes during lithium insertion and extraction process.[58]

The rate capability of the MoO_2-3DG, bulk MoO_2 and 3DG nanocomposites were investigated at various current densities as shown in Figure 4(c). The MoO_2-3DG nanocomposites were able to deliver reversible discharge capacities of 975.4, 899.1, 800.3, 716.9 and 537.3 mAh g^{-1} at the current densities of 50, 100, 200, 400, 1000 mA g^{-1}, respectively. Furthermore, the capacity was restored to a stable stage when the current density returned to 50 mAh g^{-1}. This implies that the material is highly stable and reversible. The MoO_2-3DG nanocomposites displays a better rate capability than both bulk MoO_2 and 3DG. For example, at a high current density of 1000 mA g^{-1}, bulk MoO_2 and as-prepared 3DG only delivered capacities of 99.0 mAh g^{-1} and 119.6 mAh g^{-1}, respectively, which is much lower than the 537.3 mAh g^{-1} delivered by MoO_2-3DG nanocomposites. Moreover, the rate

capability of the MoO_2-3DG nanocomposites is also better than several recently reported carbon/graphene based MoO_2 composites. For example, the MoO_2 ordered mesoporous carbon (490 mAh g^{-1} at 1000 mA g^{-1})[28], the MoO_2-multiwalled carbon nanotubes (408 mAh g^{-1} at 1000 mA g^{-1})[34] and comparable to MoO_2-graphene nanocomposites (519 mAh g^{-1} at 500 mAh g^{-1} after 60 cycles)[38]. The high rate performance could be attributed to the morphology of the anchored MoO_2 on 3DG layers which creates a short diffusion pathway for the exchange of lithium-ions and electrons from the MoO_2 nanoparticles through the well-connected 3DG network. [58]

The electrochemical impedance spectra over the frequency range of 0.01 Hz to 1 MHz of MoO_2-3DG nanocomposite, bulk MoO_2 and 3DG after various cycles were measured. Figure 5 shows the Nyquist plots for the different samples which all took similar form; a depressed semicircle in the high-middle frequency region which is related to the charge transfer resistance (R_{ct}) and an oblique straight line in the low frequency region which corresponds to Q_3, the constant phase element (CPE). When compared to bulk MoO_2, the MoO_2-3DG shows a smaller semicircle diameter (Figure 5(a)) as well as smaller R_{ct} (bulk MoO_2 64Ω versus MoO_2-3DG 27Ω) (Table S1). This suggests that latter possesses lower contact and charge-transfer resistance than the former. In Figure 5(b), the small semicircle diameters of indicates that the MoO_2-3DG nanocomposite electrodes possess low contact and charge-transfer resistance. Furthermore, it is interesting to note that the semicircle diameter decreases from cycle 1 to 100, which implies a decrease of charge-transfer resistance. This decrease could be attributed to the increase of amorphous-like structure of conductive Mo during reversible conversion MoO_2 during the activation process which is consistent with the increasing capacity over discharge and charge cycles.

4. Conclusion

Binder-free MoO_2-3DG nanocomposite electrodes have been synthesized via a facile CVD

process. MoO_2 nanoparticles were uniformly distributed anchored on the surface of 3DG layers. The binder free electrodes exhibited excellent electrochemical performance as an LIB anode material. The high specific capacity and rate performance could be ascribed to the synergistic effect between MoO_2 nanoparticles and 3DG layers which provides enhanced lithium-ion storage and facilitates fast transport of lithium ions and electrons. It is expected that the facile CVD process can be further explored to produce binder-free electrodes of several other nanocomposites with high performance for application energy storage devices.

Acknowledgements

This work is supported by SUTD-ZJU research grant ZJURP1100104. EDB-IPP PhD program is gratefully acknowledged.

References

1. A. Aricò, P. Bruce, B. Scrosati, J.-M. Tarascon and W. van Schalkwijk, *Nat. Mater.*, 2005, **4**, 366-377.
2. K. Kang, Y. S. Meng, J. Bréger, C. P. Grey and G. Ceder, *Science*, 2006, **311**, 977-980.
3. B. Scrosati, *Electrochim. Acta*, 2000, **45**, 2461-2466.
4. B. Dunn, H. Kamath and J.-M. Tarascon, *Science*, 2011, **334**, 928-935.
5. J. B. Goodenough and K. Youngsik, *Chem. Mater.*, 2010, **22**, 587-603.
6. J. Hassoun, S. Panero, P. Reale and B. Scrosati, *Adv. Mater.*, 2009, **21**, 4807-4810.
7. J. Tarascon and M. Armand, *Nature*, 2001, **414**, 359-367.
8. Y.-G. Guo, J.-S. Hu and L.-J. Wan, *Adv. Mater.*, 2008, **20**, 2878-2887.
9. J. Cabana, L. Monconduit, D. Larcher and M. Palacín, *Adv. Mater.*, 2010, **22**, E170-E192.
10. P. Poizot, S. Laruelle, S. Grugeon, L. Dupont and J. Tarascon, *Nature*, 2000, **407**, 496-499.
11. E. Vinodkumar, M. Rotem, E. Ran, S. Gregory and A. Doron, *Energy & Environmental Science*, 2011, **4**, 3243-3262.
12. Z. Wang, J. Chen, T. Zhu, S. Madhavi and X. Lou, *Chem. Commun.*, 2010, **46**, 6906-6908.
13. P. Poizot, S. Laruelle, S. Grugeon, L. Dupont and J. M. Tarascon, *J. Power Sources*, 2001, **97**, 235-239.
14. M. V. Reddy, T. Yu, C. H. Sow, Z. X. Shen, C. T. Lim, G. V. S. Rao and B. V. R. Chowdari, *Adv. Funct. Mater.*, 2007, **17**, 2792-2799.
15. Y. Wang, Z. J. Han, S. F. Yu, R. R. Song, H. H. Song, K. Ostrikov and H. Y. Yang, *Carbon*, 2013, **64**, 230-236.
16. J. H. Ku, Y. S. Jung, K. T. Lee, C. H. Kim and S. M. Oh, *J. Electrochem. Soc.*, 2009, **156**, A688-A693.
17. Y. Liang, Z. Yi, S. Yang, L. Zhou, J. Sun and Y. Zhou, *Solid State Ionics*, 2006, **177**, 501-505.
18. Y. Liang, S. Yang, Z. Yi, J. Sun and Y. Zhou, *Mater. Chem. Phys.*, 2005, **93**, 395-398.
19. L. C. Yang, Q. S. Gao, Y. Tang, Y. P. Wu and R. Holze, *J. Power Sources*, 2008, **179**, 357-360.
20. L. C. Yang, Q. S. Gao, Y. H. Zhang, Y. Tang and Y. P. Wu, *Electrochem. Commun.*, 2008, **10**, 118-122.
21. X. Zhang, X. Song, S. Gao, Y. Xu, X. Cheng, H. Zhao and L. Huo, *J. Mater. Chem. A*, 2013, **1**, 6858-6864.
22. Y. Shi, B. Guo, S. Corr, Q. Shi, Y.-S. Hu, K. Heier, L. Chen, R. Seshadri and G. Stucky, *Nano letters*, 2009, **9**, 4215-4220.
23. J. Dahn and W. Mckinnon, *Solid State Ionics*, 1987, **23**, 1-7.
24. X. Zhao, M. Cao, B. Liu, Y. Tian and C. Hu, *J. Mater. Chem.*, 2012, **22**, 13334-13340.
25. Y. Chen, X. Di, C. Ma, C. Zhu, P. Gao, J. Li, C. Sun and Q. Ouyang, *RSC Advances*, 2013, **3**, 17659-17663.
26. Y. Sun, X. Hu, W. Luo and Y. Huang, *ACS nano*, 2011, **5**, 7100-7107.
27. H.-J. Zhang, T.-H. Wu, K.-X. Wang, X.-Y. Wu, X.-T. Chen, Y.-M. Jiang, X. Wei and J.-S. Chen, *J. Mater. Chem. A*, 2013, **1**, 12038-12043.
28. L. Zeng, C. Zheng, C. Deng, X. Ding and M. Wei, *ACS applied materials & interfaces*, 2013, **5**, 2182-2187.
29. L. Yang, L. Liu, Y. Zhu, X. Wang and Y. Wu, *J. Mater. Chem.*, 2012, **22**, 13148-13152.
30. F. Ding, W. Xu, D. Choi, W. Wang, X. Li, M. H. Engelhard, X. Chen, Z. Yang and J.-G. Zhang, *J. Mater. Chem.*, 2012, **22**, 12745-12751.
31. B. Liu, X. Zhao, Y. Tian, D. Zhao, C. Hu and M. Cao, *Phys. Chem. Chem. Phys.*, 2013,

15, 8831-8837.
32. W. Luo, X. Hu, Y. Sun and Y. Huang, *Phys. Chem. Chem. Phys.*, 2011, **13**, 16735-16740.
33. L. Zhou, H. B. Wu, Z. Wang and X. W. Lou, *ACS Appl. Mater. Interfaces*, 2011, **3**, 4853-4857.
34. A. Bhaskar, M. Deepa and T. Narasinga Rao, *ACS applied materials & interfaces*, 2013, **5**, 2555-2566.
35. Y. Xu, R. Yi, B. Yuan, X. Wu, M. Dunwell, Q. Lin, L. Fei, S. Deng, P. Andersen, D. Wang and H. Luo, *J. Phys. Chem. Lett.*, 2012, **3**, 309-314.
36. P. Han, W. Ma, S. Pang, Q. Kong, J. Yao, C. Bi and G. Cui, *J. Mater. Chem. A*, 2013, **1**, 5949-5954.
37. F. Xia, X. Hu, Y. Sun, W. Luo and Y. Huang, *Nanoscale*, 2012, **4**, 4707-4711.
38. Q. Tang, Z. Shan, L. Wang and X. Qin, *Electrochim. Acta*, 2012, **79**, 148-153.
39. B. Akkisetty, D. Melepurath, T. N. Rao and U. V. Varadaraju, *J. Power Sources*, 2012, **216**, 169-178.
40. X.-C. Dong, H. Xu, X.-W. Wang, Y.-X. Huang, M. Chan-Park, H. Zhang, L.-H. Wang, W. Huang and P. Chen, *ACS nano*, 2012, **6**, 3206-3213.
41. Y. He, W. Chen, X. Li, Z. Zhang, J. Fu, C. Zhao and E. Xie, *ACS Nano*, 2013, **7**, 174-182.
42. Z. Chen, W. Ren, L. Gao, B. Liu, S. Pei and H.-M. Cheng, *Nat Mater*, 2011, **10**, 424-428.
43. X. Cao, Y. Shi, W. Shi, G. Lu, X. Huang, Q. Yan, Q. Zhang and H. Zhang, *Small*, 2011, **7**, 3163-3168.
44. X. Cao, Y. Shi, W. Shi, X. Rui, Q. Yan, J. Kong and H. Zhang, *Small*, 2013, **9**, 3433-3438.
45. J. Li, H. Dahn, L. Krause, D.-B. Le and J. Dahn, *J. Electrochem. Soc.*, 2008, **155**, A812-A816.
46. J. Luo, J. Liu, Z. Zeng, C. F. Ng, L. Ma, H. Zhang, J. Lin, Z. Shen and H. J. Fan, *Nano Lett.*, 2013, **13**, 6136-6143.
47. J. Jiang, J. Liu, S. Peng, D. Qian, D. Luo, Q. Wang, Z. Tian and Y. Liu, *J. Mater. Chem. A*, 2013, **1**, 2588-2594.
48. A. Zangwill, *Physics at Surfaces*, Cambridge University Press, 1988.
49. Q. Gao, L. Yang, X. Lu, J. Mao, Z. Yahong, Y. Wu and Y. Tang, *J. Mater. Chem.*, 2010, **20**, 2807-2812.
50. P. A. Spevack and N. S. McIntyre, *J. Phys. Chem.*, 1992, **96**, 9029-9035.
51. M. Dieterle and G. Mestl, *Phys. Chem. Chem. Phys.*, 2002, **4**, 822-826.
52. J. J. Auborn and Y. L. Barberio, *J. Electrochem. Soc.*, 1987, **134**, 638–641.
53. Y. Yang, X. Ji, F. Lu, Q. Chen and C. Banks, *Phys. Chem. Chem. Phys.*, 2013, **15**, 15098-15105.
54. A. Chen, C. Li, R. Tang, L. Yin and Y. Qi, *Phys. Chem. Chem. Phys.*, 2013, **15**, 13601-13610.
55. B. P. Vinayan, N. Rupali, V. Raman, N. Rajalakshmi, K. S. Dhathathreyan and S. Ramaprabhu, *J. Mater. Chem.*, 2012, **22**, 9949-9956.
56. L. Se-Hee, K. Yong-Hyun, D. Rohit, A. P. Philip, W. Erin, T. G. Dane, M. J. Kim, A. H. Mahan, Z. Shengbai and C. D. Anne, *Adv. Mater.*, 2008, **20**, 3627-3632.
57. Y. Sun, X. Hu, J. C. Yu, Q. Li, W. Luo, L. Yuan, W. Zhang and Y. Huang, *Energy & Environmental Science*, 2011, **4**, 2870-2877.
58. Z.-S. Wu, W. Ren, L. Wen, L. Gao, J. Zhao, Z. Chen, G. Zhou, F. Li and H.-M. Cheng, *ACS nano*, 2010, **4**, 3187-3194.

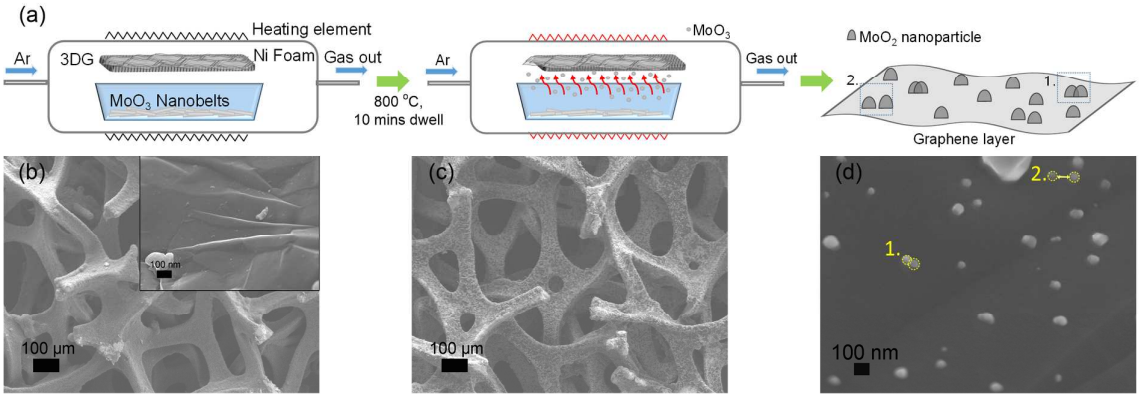

Figure 1. (a) Schematic illustration of the facile CVD process to produce MoO_2-3DG nanocomposites. (b) SEM image of as-prepared 3DG prior to MoO_2 deposition in low magnification and high magnification SEM image in inset. SEM image of MoO_2-3DG after deposition in (c) low magnification and (d) high magnification

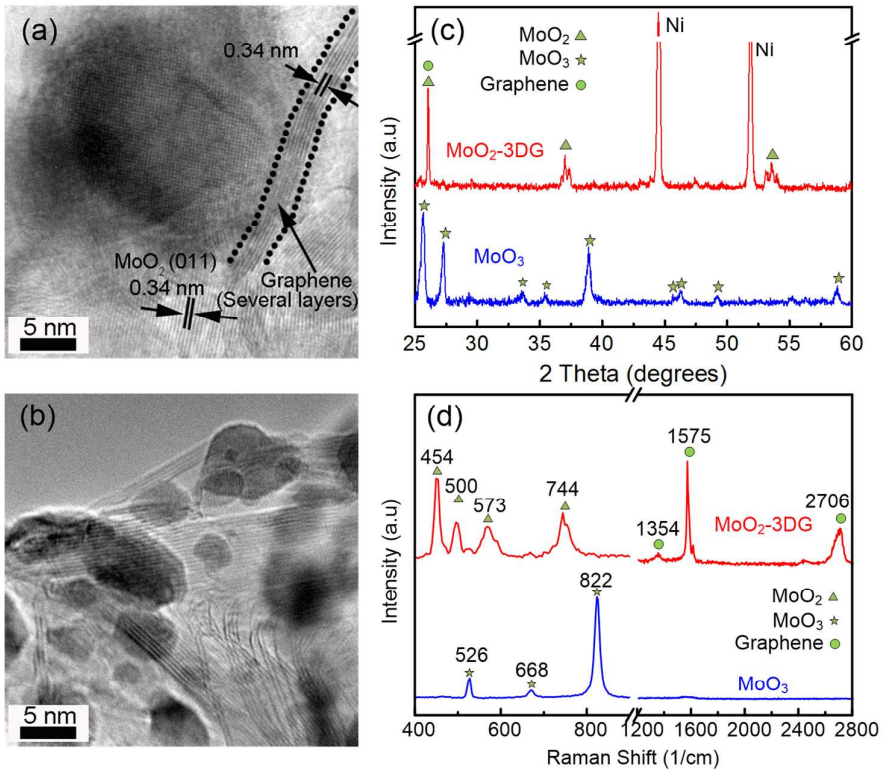

Figure 2. (a) Low and (b) High resolution TEM (HRTEM) images of MoO_2-3DG nanocomposites. (c) XRD patterns and (d) Raman spectrum of MoO_2-3DG nanocomposites and MoO_3 nanobelts.

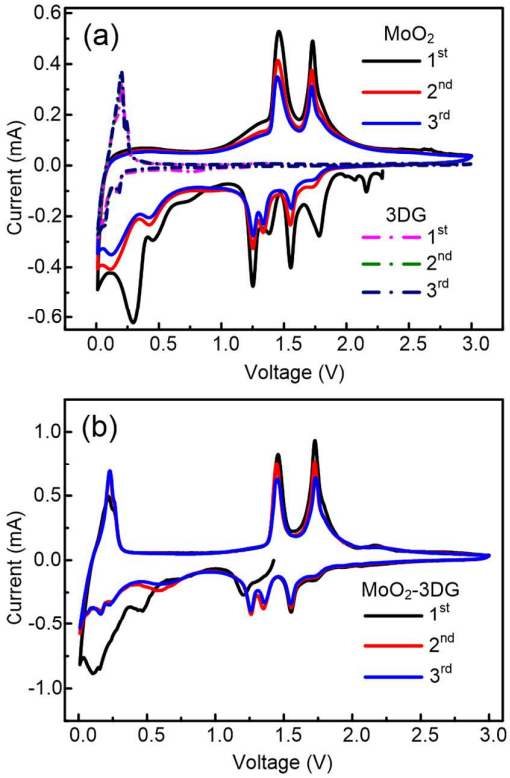

Figure 3. Cyclic voltammograms of (a) bulk MoO_2 and as-prepared 3DG, and (b) MoO_2-3DG nanocomposite electrodes at a rate of 0.05 mV/s in a potential range of 0.01 to 3.0 V.

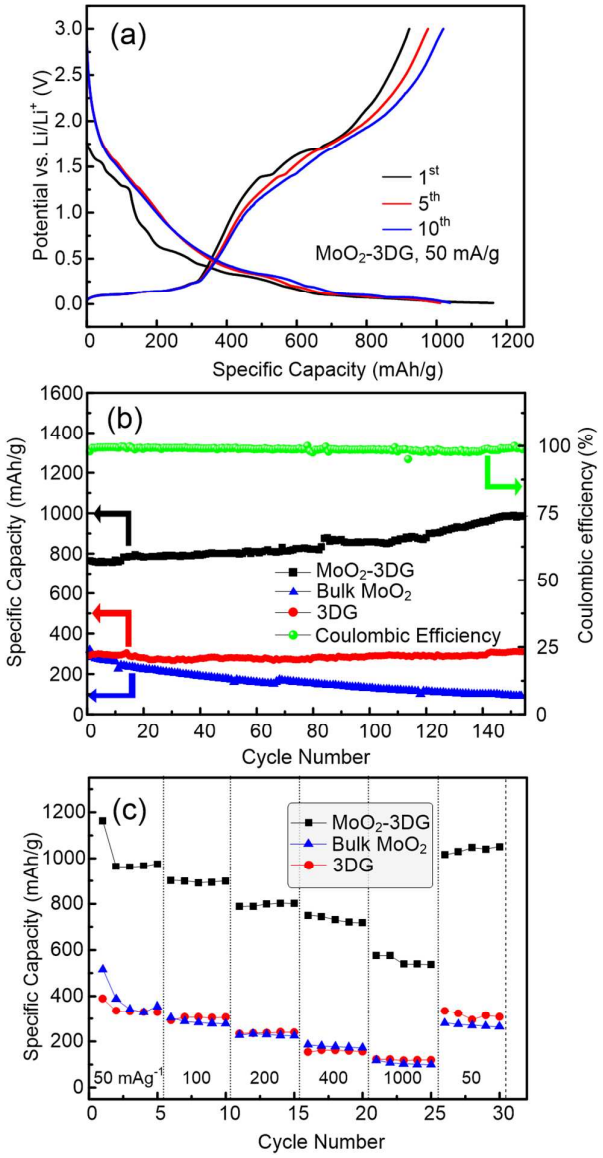

Figure 4. (a) Galvanostatic discharge and charge curves for MoO_2-3DG nanocomposite electrodes at the 1st, 5th, and 10th cycles at a current density of 50 mA g^{-1} in the potential range of 0.01 to 3.0 V. (b) Cycling performance of MoO_2-3DG nanocomposite, bulk MoO_2 and as-prepared 3DG electrodes at current density of 200 mA g^{-1}, and the corresponding coulombic efficiency of MoO_2-3DG nanocomposite electrode. (c) Rate capability of the MoO_2-3DG, bulk MoO_2 and as-prepared 3DG electrodes.

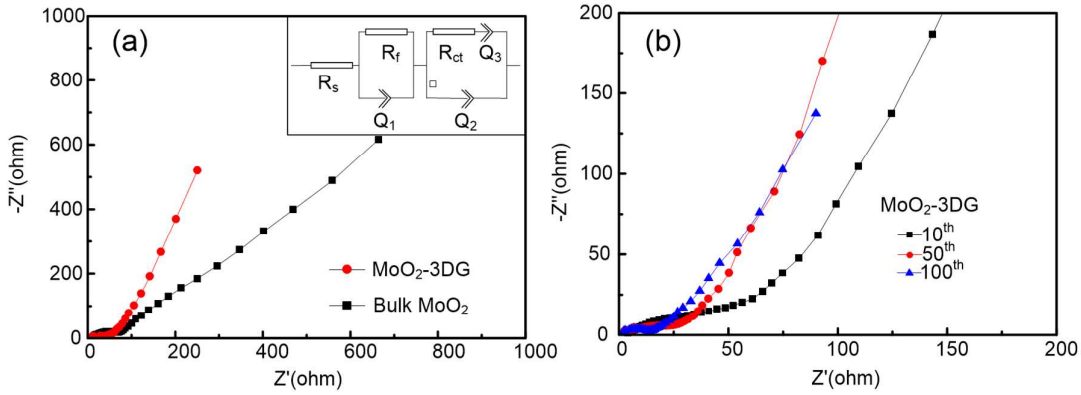

Figure 5. (a) Electrochemical impedance spectra of MoO_2-3DG nanocomposite and bulk MoO_2 electrodes. Inset shows the equivalent circuit model used for fitting. (b) Electrochemical impedance spectra of MoO_2-3DG nanocomposite electrode at various discharge and charge cycles.